ACS APPLIED ELECTRONIC MATERIALS

pubs.acs.org/acsaelm Letter

# Solution-Processable Ag-Mediated ZnO Nanowires for Scalable Low-Temperature Fabrication of Flexible Devices

Hyunsik Choi, Kwangjun Kim, Minwook Kim, Jeong Dae Kim, Incheol Cho, Inhwan Kim, Hyoungseok Chae, Inhui Han, Hyein Kim, Jung Hwan Seo, Hyoung Won Baac,* Inkyu Park,* and Jong G. Ok*

Cite This: *ACS Appl. Electron. Mater.* 2022, 4, 910–916 Read Online

ACCESS | Metrics & More | Article Recommendations | Supporting Information

**ABSTRACT:** We present a scalable and vacuum-free hybrid nanoarchitecturing strategy demonstrated by the solution-processable Ag-mediated ZnO nanowire (termed "SPAZN") growth on transparent and flexible substrates at low temperature. The SPAZN protocol enables selective hydrothermal ZnO nanowire (ZNW) growth on a nanoporous Ag framework obtainable from mild annealing of ionic Ag ink coating. The ZNW morphology and density can be readily controlled by tuning the SPAZN processing parameters including Ag ink concentration, coating condition, and hydrothermal growth temperature based on the underpinnings of the Ag-morphology-mediated ZNW growth mechanism proposed. We exemplify a transparent plastic gas sensor as one of many promising applications.

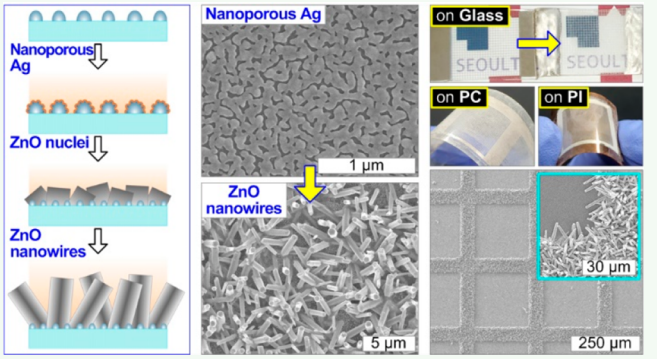


**KEYWORDS:** *low-temperature solution process, metallic nanostructure, nanowire, Ag-morphology-mediated hydrothermal growth, flexible device, gas sensor*



ZnO nanowires (ZNWs) have been extensively capitalized in various fields involving transducer, biomedical, electronic, and photonic applications because of their structural and functional versatility.[1−7] ZNWs can be grown by diverse methods, such as chemical vapor deposition (CVD) based on vapor−liquid−solid (VLS) and vapor−solid (VS) mechanisms, and by a hydrothermal reaction.[1,5,8−10] While all of these methods are effective, hydrothermal ZNW growth has the practical advantages of low-temperature and scalable processing[11,12] compared to CVD-based growth, which requires a high-temperature furnace operation, limiting the processable substrate material and area. Some typical hydrothermal growth recipes, however, demand the high-temperature (∼300−350 °C) thermal sintering of Zn-salt-based textured ZnO seed layers prior to ZNW growth,[13] which restricts the otherwise wider applications of substrate materials such as flexible plastics. Also, semiconducting ZNWs, particularly when configuring the device circuits by themselves, are often associated with a lack of conductivity and a low signal-to-noise ratio.

Accordingly, seed-free ZNW growth directly applicable to conductive frameworks such as metal layers[14−16] and conductive nanomaterials (e.g., carbon nanotubes (CNTs)[8,9] and graphene[17,18]) can be a highly promising strategy toward functional hybrid nanodevices. Taking this one step further, avoiding the use of high-temperature and/or vacuum-assisted instruments during the preparation of such conductive metallic supports may further extend the scalability, productivity, and applicability of flexible and scalable ZNW-based device systems.

To this end, the solution-processable Ag nanostructure (SPAN) which can be fabricated in a vacuum-free and scalable fashion through the simple coating and much milder annealing (i.e., at ∼120−180 °C) of an ionic Ag ink[19,20] can provide a suitable framework for ZNWs. More remarkably, the SPAN film could replace the textured ZnO seed for reliable hydrothermal ZNW growth, as preliminarily noted in earlier studies.[10,13] The present work will shed light on how ZNW growth is controlled by the SPAN morphology, which can be readily tuned by the ionic Ag ink concentration and coating condition. A specific prior study of seed-free ZNW growth on conventional vacuum-evaporated Ag film may provide us with the underpinnings of the Ag-morphology-mediated ZNW growth mechanism, which can be directly applied to the

**Received:** January 8, 2022
**Accepted:** February 17, 2022
**Published:** February 17, 2022

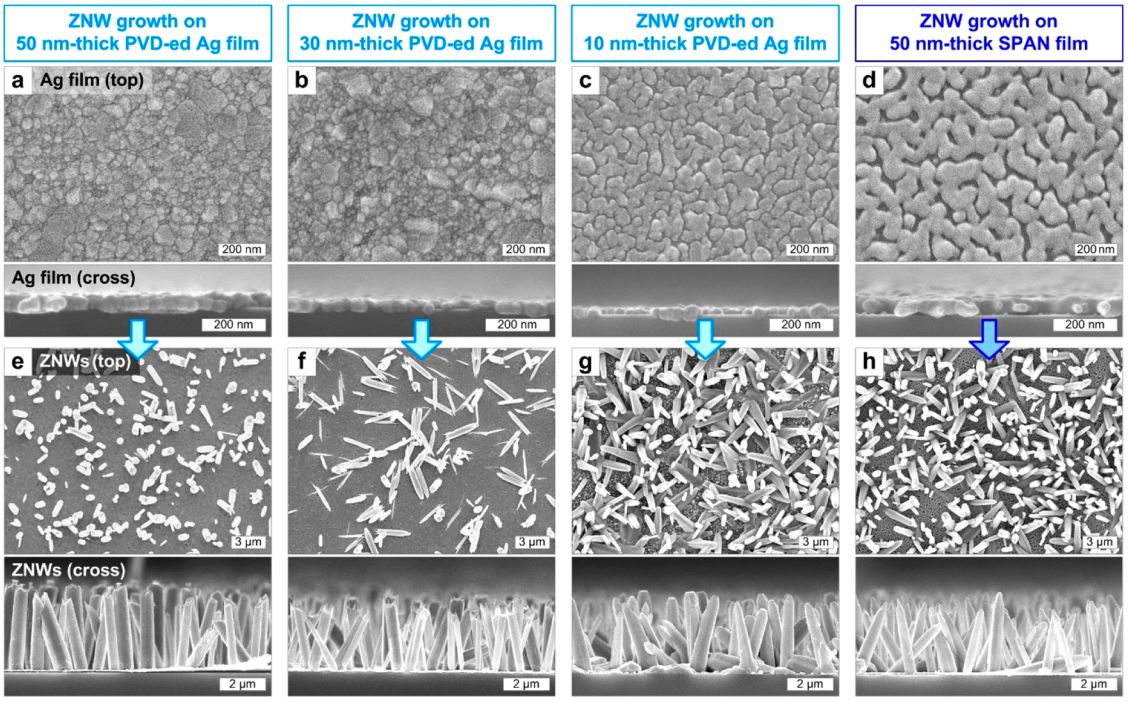


**Figure 1.** Top-view and cross-sectional SEM images of Ag films (a–d) deposited by PVD or the SPAN protocol and ZNWs (e–h) grown on the corresponding Ag films through the hydrothermal process. The Ag film thickness for each case is denoted on the top row.

SPAN framework processable on flexible polymer substrates at a low temperature. We demonstrate that this solution-processable Ag-mediated ZNW (SPAZN) architecturing strategy enables the general application of flexible devices consisting of electrically addressable ZNWs on conductive frameworks, as exemplified by the plastic gas sensors presented here.

We initially investigated the hydrothermal ZNW growth on the Ag layers vacuum-evaporated with varied thicknesses, and on the SPAN layer, to understand the physical morphology-dependent ZNW growth features. The detailed experimental conditions for Ag film deposition and hydrothermal ZNW growth are described in the Supporting Information. Briefly, for the SPAN film coating, the ionic Ag ink was mixed with isopropyl alcohol (IPA) at a volume ratio of 1:1. This 50 vol % diluted in IPA ionic Ag ink (simply the "50% Ag ink" hereafter) was then spin-coated at 2000 rpm for 20 s, followed by soft baking (90 °C, 1 min) and hard baking (180 °C, 5 min) unless otherwise specified. For hydrothermal ZNW growth, the Ag-coated substrate was immersed in an aqueous precursor solution containing 25 mM $Zn(NO_3)_2$ and 25 mM hexamethylenetetramine (HMTA; $(CH_2)_6N_4$) and was treated at 90 °C for 15 h in an oven. Figure 1 shows scanning electron microscope (SEM) images of ZNWs (Figures 1e–h) grown on Ag films deposited onto Si substrates by physical vapor deposition (PVD; e-beam evaporation) with thicknesses of 50, 30, and 10 nm (Figures 1a–c) and by the SPAN protocol with an approximate thickness of 50 nm (Figure 1d). The ZNW length, typically controllable by the growth time,[10,13] is found to be almost identical (~3.3–3.5 $\mu$m) regardless of the Ag film thickness, with the ZNW diameter distribution of ~600–800 nm. However, clearly observable is that the ZNWs are grown more conformally with a higher density on the thinner PVD-ed Ag film and on the SPAN film. For clarification, the areal ZNW densities of the four cases are quantitatively examined by analyzing the SEM images shown in Figures 1e, 1f, 1g, and 1h; the numbers of ZNWs per unit area of 100 $\mu m^2$ are found to be 65, 44, 102, and 95, respectively, confirming the observation. Interestingly, the 10 nm thick PVD-ed Ag film (Figure 1c) and the SPAN film (Figure 1d) reveal similar nanoporous morphologies prior to ZNW growth, whereas the thicker PVD-ed Ag films (i.e., 50 and 30 nm thicknesses; Figures 1a,b) show denser and more continuous layer textures.

These outcomes suggest that the structural morphology of the Ag layer, in conjunction with the Ag-seeded chemical reaction, would play an important role in facilitating ZNW growth. There may be several physical factors that vary according to the nanoporosity of the Ag film; as the Ag film becomes more porous, both the overall surface area and the "sidewall" region increase. Also notably, the following chemical reaction procedure occurs during Ag-seeded hydrothermal ZNW growth; the native oxides of Ag (i.e., $Ag_2O$ and other Ag–O complexes), typically formed to a thickness of 1–2 nm,[21] are positively ionized in the $Zn(NO_3)_2$-dissolved precursor solution; the precursor solution is generally alkaline because of the addition of amine base, HMTA, leading Zn species to form $OH^-$-rich, negatively charged complexes (e.g., $Zn(OH)_3^-$ and $Zn(OH)_4^{2-}$);[10,13,16] the positively charged Ag surface is thus favorable for binding the negatively charged Zn complexes, thereby promoting ZNW growth. Figure 2 schematically illustrates the nanoporous Ag-mediated ZNW growth model considering the aforementioned perspectives. For the condensed Ag film (e.g., 50 nm thick PVD-ed film), only the top surface is exposed to the precursor solution (Figure 2a). In contrast, for the more porous Ag films (e.g., 10 nm thick PVD-ed and SPAN films; Figure 2b), the sidewall area along with the top surface also interacts with the Zn species in the solution, which may activate the formation of a larger number of ZnO nuclei. This accordingly increases the growth of the ZnO crystal grains, leading to ZNW growth with


https://doi.org/10.1021/acsaelm.2c00035
ACS Appl. Electron. Mater. 2022, 4, 910–916

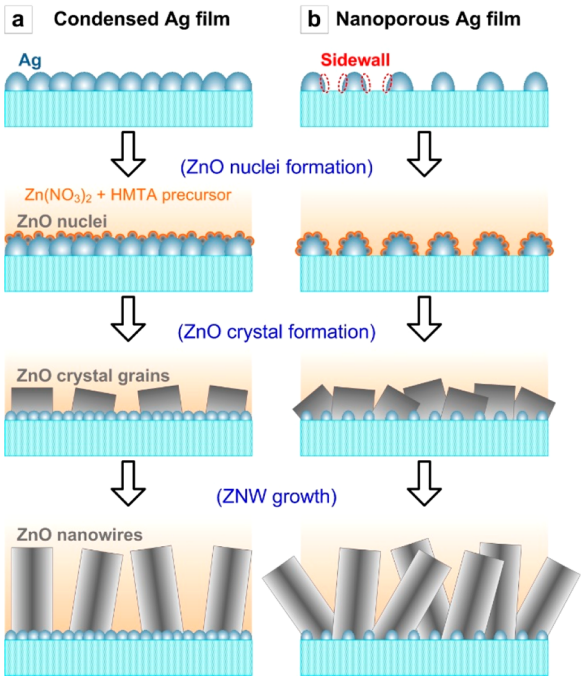


**Figure 2.** Schematic procedure of the solution-processable Ag-mediated ZNW (SPAZN) growth on the (a) condensed Ag film and (b) nanoporous Ag film. ZnO crystals grow by the diffusive merging of the ZnO nuclei formed on the Ag surface exposed to the precursor solution, evolving into ZNWs along the energetically favorable direction.

a higher density. Here, it is important to note that the average diameter of ZNWs is found to be greater overall than the average size of the individual Ag nanoclusters; this likely indicates that the initially formed ZnO nuclei can diffuse actively on the Ag surface and agglomerate to form larger crystal clusters, which can be kinetically led by Ostwald ripening in an energetically favorable manner.[22,23] Another effect of the sidewall is to assist the progress of conformal ZNW growth by providing numerous topographic orientations to the wurtzite ZnO crystals from which ZNWs grow along the energetically favorable *c*-axis (i.e., [0001] direction).[10]

Such an Ag-morphology-mediated ZNW growth mechanism indicates that the ZNW density and morphology can be tailored by controlling the Ag film thickness and porosity. This can be readily conducted by adjusting the Ag ink concentration and corresponding spin-coating speed in the SPAZN architecturing strategy in a much more facile, scalable, and productive fashion than relying on PVD. Figure 3 shows SEM image matrices of SPAN and SPAZN samples fabricated under parametrically controlled Ag ink concentrations (i.e., 25% and 50%) and coating speed conditions (i.e., 1000 and 2000 rpm). While the nanoporous SPAN layers (Figures 3a–d) resulted generally in conformal ZNW growth (Figures 3e–h), the ZNW morphology and density can be apparently tuned depending on the initial SPAN morphology and porosity. Specifically, when the SPAN porosity is too high (Figure 3a), the ZnO nanostructure is found to be less uniform with an increased number of non-NW-shaped clusters (Figure 3e). In this case, the vast Ag sidewall area out of superfluous pores likely induces excessive nucleation and growth of randomly oriented ZnO crystals, some of which may agglomerate rather than individually initiate ZNW growth. Conversely, when the

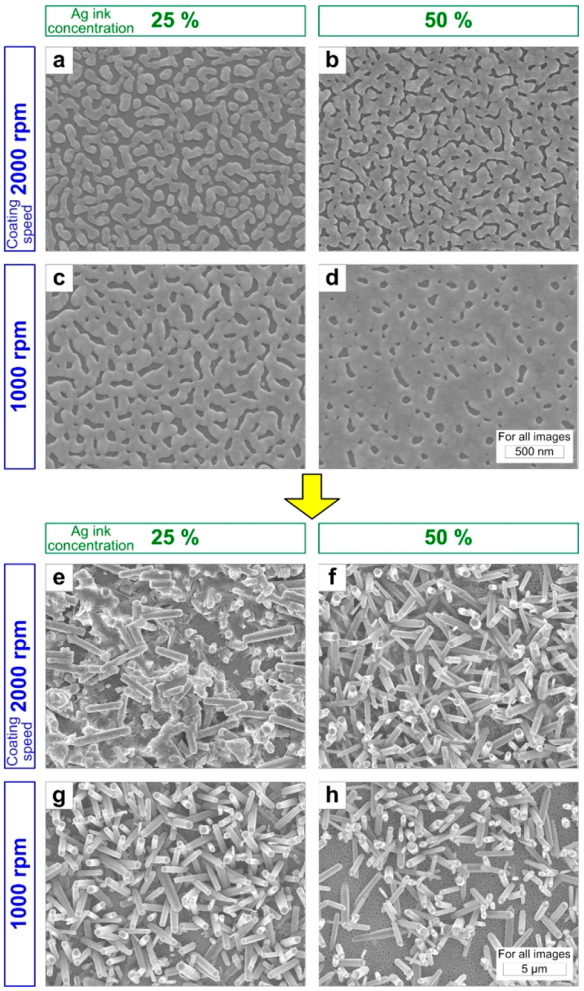


**Figure 3.** (a–d) SEM images of SPAN surfaces fabricated by the spin-coating of the 25% and 50% Ag ink solutions at 2000 and 1000 rpm, followed by mild thermal annealing. (e–h) SEM images of SPAZN structures grown on the corresponding SPAN surfaces.

SPAN film becomes denser (Figure 3d), the ZNW density decreases (Figure 3h). This is consistent with the above-mentioned SPAZN growth mechanism. As shown in Figures 3f,g, the high-density conformal ZNWs can be uniformly grown on the SPAN layers, providing moderate pore and sidewall density levels controllable with the balance of the Ag ink concentration and coating speed (Figures 3b,c).

The hydrothermal ZNW growth temperature is another essential factor to consider when attempting to modulate the SPAZN structure in terms of the aspect ratio of individual ZNWs as well as the overall ZNW density. Figures 4a–c show SEM images of SPAZN structures grown at three different temperatures of 80, 90, and 100 °C, all on SPAN layers prepared by using 50% Ag ink spin-coated at 2000 rpm (simply termed the "50%–2000 rpm SPAN" hereafter) for 15 h. First, it can be found that the ZNWs are grown with a higher density and length at 90 °C (Figure 4b) compared to the outcomes at other growth temperatures. Another notable finding is that the average ZNW diameter decreases when the growth temperature increases to 100 °C. By analysis of 100 ZNWs for each case, the average lengths and diameters were measured and found to be 2.72, 3.48, and 3.11 $\mu$m (for length) and 913, 782, and 566 nm (for diameter). The corresponding aspect ratios can be accordingly approximated to be 2.98, 4.45, and 5.49,


https://doi.org/10.1021/acsaelm.2c00035
ACS Appl. Electron. Mater. 2022, 4, 910–916

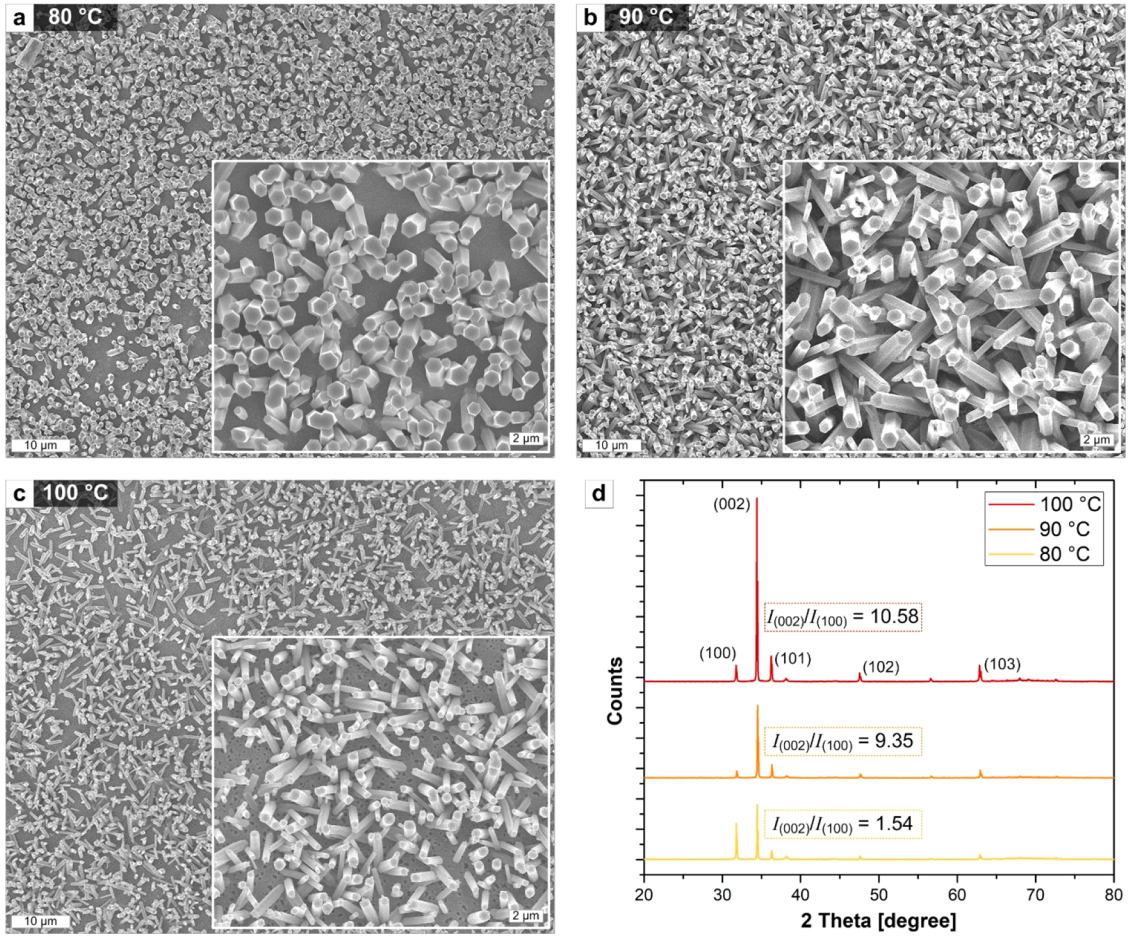


**Figure 4.** SEM images of SPAZN structures grown at (a) 80, (b) 90, and (c) 100 °C. The insets show enlarged views of the corresponding structures. (d) XRD spectra of SPAZN structures grown at three different temperatures. The corresponding $I_{(002)}/I_{(100)}$ values are indicated beside each spectrum.

respectively. Additionally, hexagonal facets distinctly appear, especially in the ZNWs grown with larger diameters (e.g., 80 °C growth case; Figure 4a). Thermal energy provided during the given growth time facilitates the progress of the thermodynamically driven hydrothermal reaction, which can provide a reasonable basis for the more active SPAZN growth at 90 °C compared to 80 °C. However, too high a growth temperature (e.g., 100 °C) can impede ZNW growth initiated from ionic bonds. This may partly stem from increased solubility of the ionic species in the precursor solution.

An X-ray diffraction analysis (XRD) provides additional insight into the crystalline quality and structural characteristics of the SPAZN structures. Figure 4d plots the XRD spectra of SPAZN structures grown at 80, 90, and 100 °C. Sharp and narrow (002) peaks are dominant, indicating that highly crystalline ZNWs grow along the *c*-axis of the wurtzite ZnO crystal.[13] The (100) peak that emerges from the hexagonal side facets[24,25] is vivid, especially in the 80 °C-grown SPAZN, as confirmed in the SEM image (Figure 4a). It is noteworthy that the ratio of the (002) peak intensity to the (100) peak intensity ($I_{(002)}/I_{(100)}$) can be an indicator of the aspect ratio of the ZNWs;[24] the higher the ratio, the higher the ZNW aspect ratio. The corresponding $I_{(002)}/I_{(100)}$ values of the three cases calculated and marked in Figure 4d indicate that the aspect ratios of the ZNWs can be controlled to be highest and lowest at 100 and 80 °C, respectively, during our SPAZN growth process. This is consistent with the experimental measurement result given above.

The SPAZN architecturing strategy in which ZNWs with controlled morphologies can be grown selectively on Ag patterns at a temperature can be directly applied to the development of a variety of practical devices with transparent and flexible forms. As one tangible example, we demonstrate transparent and flexible gas sensors obtainable from SPAZN structures patterned on a diverse range of common substrates, including polycarbonate (PC), polyimide (PI), and glass. Figure 5 presents the collective results of the micropatterned flexible SPAZN structures and their application to the transparent gas sensors. As an effective and transparent sensing circuit, 25%−1000 rpm SPAN layers of ∼50 nm thickness were initially engineered into micromesh patterns through photolithography followed by wet etching. The optical transmittance and electrical conductivity of the SPAN micromesh structure can be controlled by varying its unit cell size ($S$) and line width ($L$) (see the inset of Figure 5c), as previously studied in detail.[19] Here, we designed two types of SPAN micromeshes with the $S/L$ values of 500/50 $\mu$m and 250/50 $\mu$m (simply termed the "500/50 and 250/50 micromeshes" below) onto which ∼4 $\mu$m long ZNWs were selectively grown at 90 °C for 15 h to complete the SPAZN structures. Figure 5a exhibits the exemplary procedure for the fabrication of transparent and flexible SPAZN devices beginning with the 500/50 and/or



https://doi.org/10.1021/acsaelm.2c00035
ACS Appl. Electron. Mater. 2022, 4, 910−916

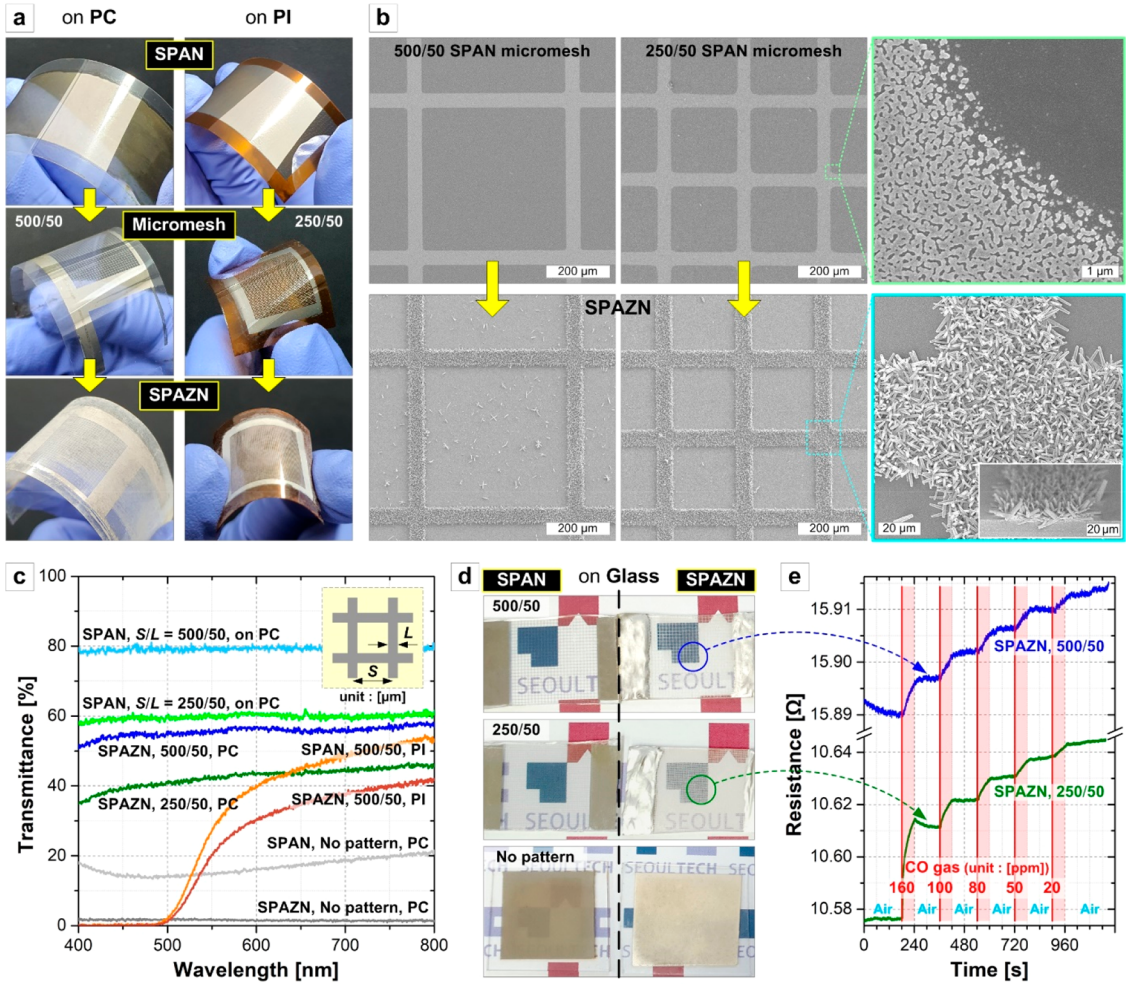


**Figure 5.** (a) Stepwise optical images of micromesh-patterned SPAZN structures fabricated on PC and PI substrates. (b) SEM images of the 500/50 and 250/50 SPAN micromesh structures (top row) and the SPAZN structures grown on them (bottom row). The right-side images show enlarged views of the Ag−substrate boundary area (top right) and the SPAZN micromesh's crossing area with the cross-sectional view as an inset (bottom right). (c) Optical transmittances measured for the 500/50 and 250/50 micromesh-patterned SPAN and SPAZN structures (and nonpatterned ones as references) fabricated on various transparent substrates. (d) Optical images of the 500/50 and 250/50 SPAN and SPAZN micromesh structures fabricated on glass substrates and (e) the CO gas-sensing performances of these SPAZN structures. CO gas with various concentrations was introduced for the red-shaded timespans marked in the plot, while purified air was introduced between these timespans.

250/50 micromesh-patterned SPAN layers formed on the PC and PI substrates. The SEM images (Figure 5b) clearly indicate that the ZNWs are highly selectively grown on the Ag patterns, corroborating Ag-mediated ZNW growth in the SPAZN architecturing protocol.

Figure 5c shows the measured optical transmittances of the 500/50 and/or 250/50 micromesh-patterned SPAZN structures formed on various transparent substrates. The sensing ability of these architectures was characterized by introducing dry CO gas at various concentrations onto the SPAZN micromesh-on-glass samples (Figure 5d) at room temperature and ∼0% relative humidity. Figure 5e shows the measurement result upon changes in the resistance of these SPAZN samples depending on the CO gas concentration, demonstrating their reliable performance as transparent gas sensors. The CO gas sensing systems employing metal oxide materials such as ZnO, CuO, $SnO_2$, and $MoS_2$ as well as their various nanostructures[26−28] may inspire the future improvement of SPAZN-based gas sensor devices. Moving forward, the SPAZN architecturing strategy may also be adopted to more practical device systems of broader functionalities including other pollutant detection,[29−31] catalytic reaction,[24] and electromechanical transduction,[32] among others. This will be realized by regulating additional process parameters, such as the precursor composition and growth time, by diversifying the framework architectures (e.g., ZNW-connected interdigitated electrodes) and/or by incorporating complementary materials. Indeed, a roll-to-roll-processed interdigital transducer comprising the SPAZN architecture and the microelectrode fabricated by rollable photolithography[33,34] is currently under development. This may exploit a new route to "all-solution-processable" and the continuous manufacturing of flexible large-area utility devices with versatile functions involving CO/$NH_3$ gas sensing and optoelectronic transduction.

In summary, we developed a scalable SPAZN architecturing protocol by which ZNWs can be selectively grown on a SPAN framework at a low temperature without using costly vacuum-processing instruments. Based on the proposed Ag-morphology-mediated growth mechanism, the ZNW morphology, density, and aspect ratio could be facilely controlled by the initial Ag ink concentration and corresponding spin-coating speed and the hydrothermal growth condition. Our demon-


https://doi.org/10.1021/acsaelm.2c00035
ACS Appl. Electron. Mater. 2022, 4, 910−916

stration of patterned SPAZN growth on glass and polymeric substrates bodes well for the practical manufacturing of various transparent and flexible devices. While we exemplified a room-temperature-operational gas sensor in this work, more diverse functional applications can be realized by utilizing the SPAZN architectures, including but not limited to low-cost sensor networks and wearable devices, large-area transparent electronics, and flexible plasmonic and transducer elements.

## ■ ASSOCIATED CONTENT

### Supporting Information

The Supporting Information is available free of charge at https://pubs.acs.org/doi/10.1021/acsaelm.2c00035.

Experimental methods: fabrication and characterization details (PDF)

## ■ AUTHOR INFORMATION


### Corresponding Authors

**Hyoung Won Baac** − *Department of Electrical and Computer Engineering, Sungkyunkwan University, Suwon 16419, Republic of Korea*; Phone: +82-31-299-4327; Email: hwbaac@skku.edu

**Inkyu Park** − *Department of Mechanical Engineering, Korea Advanced Institute of Science and Technology (KAIST), Daejeon 34141, Republic of Korea*; orcid.org/0000-0001-5761-7739; Phone: +82-42-350-7922; Email: inkyu@kaist.ac.kr

**Jong G. Ok** − *Department of Mechanical and Automotive Engineering, Seoul National University of Science and Technology, Seoul 01811, Republic of Korea*; orcid.org/0000-0002-8703-2915; Phone: +82-2-970-9012; Email: jgok@seoultech.ac.kr

### Authors

**Hyunsik Choi** − *Department of Mechanical and Automotive Engineering, Seoul National University of Science and Technology, Seoul 01811, Republic of Korea*

**Kwangjun Kim** − *Department of Mechanical and Automotive Engineering, Seoul National University of Science and Technology, Seoul 01811, Republic of Korea*

**Minwook Kim** − *Department of Mechanical and Automotive Engineering, Seoul National University of Science and Technology, Seoul 01811, Republic of Korea*

**Jeong Dae Kim** − *Department of Mechanical and Automotive Engineering, Seoul National University of Science and Technology, Seoul 01811, Republic of Korea;* Present Address: Etch Team, SEMES Co., Ltd., 77 4-Sandan 5-gil, Jiksan-eup, Seobuk-gu, Cheonan, Chungcheongnam-do 31040, Republic of Korea

**Incheol Cho** − *Department of Mechanical Engineering, Korea Advanced Institute of Science and Technology (KAIST), Daejeon 34141, Republic of Korea*

**Inhwan Kim** − *Department of Mechanical and Automotive Engineering, Seoul National University of Science and Technology, Seoul 01811, Republic of Korea;* Present Address: Korea Airports Corp., 980 Ochang-daero, Naesu-eup, Cheongwon-gu, Chungcheongbuk-do 28142, Republic of Korea

**Hyoungseok Chae** − *Department of Mechanical and Automotive Engineering, Seoul National University of Science and Technology, Seoul 01811, Republic of Korea*

**Inhui Han** − *Department of Mechanical and Automotive Engineering, Seoul National University of Science and Technology, Seoul 01811, Republic of Korea*

**Hyein Kim** − *Department of Mechanical and Automotive Engineering, Seoul National University of Science and Technology, Seoul 01811, Republic of Korea*

**Jung Hwan Seo** − *Department of Mechanical & System Design Engineering, Hongik University, Seoul 04066, Republic of Korea*

Complete contact information is available at: https://pubs.acs.org/10.1021/acsaelm.2c00035


### Author Contributions

H. Choi, K.K., and M.K. contributed equally to this work. H. Choi, J.D.K., and J.G.O. conceived the principle and designed the research, with useful advice from H.W.B. and I.P. for characterization and device application. H. Choi, K.K., and M.K. conducted most of the experiments and characterizations, J.D.K., I.K., H. Chae, I.H., and H.K. contributed to the parametric experiment and result interpretation, and I.C. helped conduct the device measurements, under the supervision of J.H.S., I.P., and J.G.O. and with the useful instruction from H.W.B. H. Choi, K.K., M.K., and J.G.O. wrote the manuscript with all authors' assistance with figure preparation and consistent discussion. All authors read and approved the final manuscript.

### Notes

The authors declare no competing financial interest.

## ■ ACKNOWLEDGMENTS

This work was supported by grants from the National Research Foundation of Korea (NRF) funded by the Korean Government (No. 2020R1F1A1073760 and No. 2021M3H4A3A02099204 (Ministry of Science and ICT (MSIT)). We thank Wonseok Lee, Minyoung Lee, Kangeun Yoo, and Hyeonmin Shin for their assistance with the prior experiment and additional characterization processes.

## ■ REFERENCES


(1) Noman, M. T.; Amor, N.; Petru, M. Synthesis and applications of ZnO nanostructures (ZONSs): a review. *Crit. Rev. Solid State Mater. Sci.* **2021**, 1.

(2) Goel, S.; Kumar, B. A review on piezo-/ferro-electric properties of morphologically diverse ZnO nanostructures. *J. Alloys Compd.* **2020**, *816*, 152491.

(3) Kang, Y. L.; Yu, F.; Zhang, L.; Wang, W. H.; Chen, L.; Li, Y. C. Review of ZnO-based nanomaterials in gas sensors. *Solid State Ionics* **2021**, *360*, 115544.

(4) Li, X. S.; Liu, X.; Li, Y. D.; Gao, D. H.; Cao, L. Z. Using Novel Semiconductor Features to Construct Advanced ZnO Nanowires-Based Ultraviolet Photodetectors: A Brief Review. *Ieee Access* **2021**, *9*, 11954−11973.

(5) Le, A. T.; Ahmadipour, M.; Pung, S. Y. A review on ZnO-based piezoelectric nanogenerators: Synthesis, characterization techniques, performance enhancement and applications. *J. Alloys Compd.* **2020**, *844*, 156172.

(6) Ijaz, M.; Zafar, M.; Islam, A.; Afsheen, S.; Iqbal, T. A Review on Antibacterial Properties of Biologically Synthesized Zinc Oxide Nanostructures. *Journal of Inorganic and Organometallic Polymers and Materials* **2020**, *30* (8), 2815−2826.

(7) Galdamez-Martinez, A.; Santana, G.; Güell, F.; Martinez-Alanis, P. R.; Dutt, A. Photoluminescence of ZnO Nanowires: A Review. *Nanomaterials* **2020**, *10* (5), 857.

(8) Ok, J. G.; Tawfick, S. H.; Juggernauth, K. A.; Sun, K.; Zhang, Y. Y.; Hart, A. J. Electrically Addressable Hybrid Architectures of Zinc Oxide Nanowires Grown on Aligned Carbon Nanotubes. *Adv. Funct. Mater.* **2010**, *20* (15), 2470−2480.
(9) Ok, J. G.; Lee, J. Y.; Baac, H. W.; Tawfick, S. H.; Guo, L. J.; Hart, A. J. Rapid Anisotropic Photoconductive Response of ZnO-Coated Aligned Carbon Nanotube Sheets. *ACS Appl. Mater. Interfaces* **2014**, *6* (2), 874−881.
(10) Oh, D. K.; Choi, H.; Shin, H.; Kim, K.; Kim, M.; Ok, J. G. Tailoring zinc oxide nanowire architectures collectively by catalytic vapor-liquid-solid growth, catalyst-free vapor-solid growth, and low-temperature hydrothermal growth. *Ceram. Int.* **2021**, *47* (2), 2131−2143.
(11) Burke-Govey, C. P.; Plank, N. O. V. Review of hydrothermal ZnO nanowires: Toward FET applications. *J. Vac. Sci. Technol. B* **2013**, *31* (6), 06F101.
(12) Qin, L. G.; Mawignon, F. J.; Hussain, M.; Ange, N. K.; Lu, S.; Hafezi, M.; Dong, G. N. Economic Friendly ZnO-Based UV Sensors Using Hydrothermal Growth: A Review. *Materials* **2021**, *14* (15), 4083.
(13) Yoo, K.; Lee, W.; Kang, K.; Kim, I.; Kang, D.; Oh, D. K.; Kim, M. C.; Choi, H.; Kim, K.; Kim, M.; Kim, J. D.; Park, I.; Ok, J. G. Low-temperature large-area fabrication of ZnO nanowires on flexible plastic substrates by solution-processible metal-seeded hydrothermal growth. *Nano Convergence* **2020**, DOI: 10.1186/s40580-020-00235-6.
(14) Wen, X.; Wu, W.; Ding, Y.; Wang, Z. L. Seedless synthesis of patterned ZnO nanowire arrays on metal thin films (Au, Ag, Cu, Sn) and their application for flexible electromechanical sensing. *J. Mater. Chem.* **2012**, *22* (19), 9469−9476.
(15) Huang, H.; Wang, H.; Li, B.; Mo, X.; Long, H.; Li, Y.; Zhang, H.; Carroll, D. L.; Fang, G. Seedless synthesis of layered ZnO nanowall networks on Al substrate for white light electroluminescence. *Nanotechnology* **2013**, *24* (31), 315203.
(16) Kim, B. H.; Kwon, J. W. Metal Catalyst for Low-Temperature Growth of Controlled Zinc Oxide Nanowires on Arbitrary Substrates. *Sci. Rep.* **2015**, DOI: 10.1038/srep04379.
(17) Zou, R.; He, G.; Xu, K.; Liu, Q.; Zhang, Z.; Hu, J. ZnO nanorods on reduced graphene sheets with excellent field emission, gas sensor and photocatalytic properties. *J. Mater. Chem. A* **2013**, *1* (29), 8445−8452.
(18) Cook, B.; Liu, Q.; Liu, J.; Gong, M.; Ewing, D.; Casper, M.; Stramel, A.; Wu, J. Facile zinc oxide nanowire growth on graphene via a hydrothermal floating method: towards Debye length radius nanowires for ultraviolet photodetection. *J. Mater. Chem. C* **2017**, *5* (38), 10087−10093.
(19) Kim, J. D.; Choi, H.; Kim, K.; Chae, H.; Yi, H.; Jeong, M. H.; Lee, N.; Lee, M.; Kim, M. C.; Suk, J. W.; Lee, K.-T.; Jeong, H. E.; Ok, J. G. Ionic solution-processable Ag nanostructures with tunable optical and electrical properties and strong adhesion to general substrates. *Applied Materials Today*, under review.
(20) Wi, J. S.; Kim, J. D.; Lee, W.; Choi, H.; Kwak, M.; Song, J.; Lee, T. G.; Ok, J. G. Inkjet-Printable Nanoporous Ag Disk Arrays Enabling Coffee-Ring Effect-Driven Analyte Enrichment Towards Practical SERS Applications. *International Journal of Precision Engineering and Manufacturing-Green Technology*.
(21) Derooij, A. The Oxidation of Silver by Atomic Oxygen. *Esa Journal-European Space Agency* **1989**, *13* (4), 363−382.
(22) Wong, E. M.; Bonevich, J. E.; Searson, P. C. Growth kinetics of nanocrystalline ZnO particles from colloidal suspensions. *J. Phys. Chem. B* **1998**, *102* (40), 7770−7775.
(23) Talapin, D. V.; Rogach, A. L.; Haase, M.; Weller, H. Evolution of an ensemble of nanoparticles in a colloidal solution: Theoretical study. *J. Phys. Chem. B* **2001**, *105* (49), 12278−12285.
(24) Takeuchi, M.; Koba, T.; Matsuoka, M. Fabrication of Ag/ZnO nanowire thin films and their photocatalytic reactivities. *Res. Chem. Intermed.* **2020**, *46* (11), 4883−4896.
(25) Urs, K. M. B.; Kamble, V. Surface photovoltage response of zinc oxide microrods on prismatic planes: effect of UV, temperature and oxygen ambience. *Journal of Materials Science-Materials in Electronics* **2021**, *32* (5), 6414−6424.
(26) Zhang, D.; Jiang, C.; Liu, J.; Cao, Y. Carbon monoxide gas sensing at room temperature using copper oxide-decorated graphene hybrid nanocomposite prepared by layer-by-layer self-assembly. *Sens. Actuators, B* **2017**, *247*, 875−882.
(27) Zhang, D.; Sun, Y.; Jiang, C.; Yao, Y.; Wang, D.; Zhang, Y. Room-temperature highly sensitive CO gas sensor based on Ag-loaded zinc oxide/molybdenum disulfide ternary nanocomposite and its sensing properties. *Sens. Actuators, B* **2017**, *253*, 1120−1128.
(28) Yang, Z.; Zhang, D.; Wang, D. Carbon monoxide gas sensing properties of metal-organic frameworks-derived tin dioxide nanoparticles/molybdenum diselenide nanoflowers. *Sens. Actuators, B* **2020**, *304*, 127369.
(29) Zhang, D.; Wu, J.; Cao, Y. Ultrasensitive $H_2S$ gas detection at room temperature based on copper oxide/molybdenum disulfide nanocomposite with synergistic effect. *Sens. Actuators, B* **2019**, *287*, 346−355.
(30) Zhang, D.; Yang, Z.; Li, P.; Pang, M.; Xue, Q. Flexible self-powered high-performance ammonia sensor based on Au-decorated $MoSe_2$ nanoflowers driven by single layer $MoS_2$-flake piezoelectric nanogenerator. *Nano Energy* **2019**, *65*, 103974.
(31) Wang, D.; Zhang, D.; Guo, J.; Hu, Y.; Yang, Y.; Sun, T.; Zhang, H.; Liu, X. Multifunctional poly(vinyl alcohol)/Ag nanofibers-based triboelectric nanogenerator for self-powered MXene/tungsten oxide nanohybrid $NO_2$ gas sensor. *Nano Energy* **2021**, *89*, 106410.
(32) Woo, H. K.; Kim, H.; Jeon, S.; Lee, W. S.; Ahn, J.; Bang, J.; Kang, M. S.; Oh, S. J. One-step chemical treatment to design an ideal nanospacer structure for a highly sensitive and transparent pressure sensor. *J. Mater. Chem. C* **2019**, *7* (17), 5059−5066.
(33) Ok, J. G.; Kwak, M. K.; Huard, C. M.; Youn, H. S.; Guo, L. J. Photo Roll Lithography (PRL) for continuous and scalable patterning with application in flexible electronics. *Adv. Mater.* **2013**, *25* (45), 6554−6561.
(34) Lee, S. H.; Kim, S. W.; Park, C. W.; Jeong, H. E.; Ok, J. G.; Kwak, M. K. Scalable fabrication of flexible transparent heaters comprising continuously created metallic micromesh patterns incorporated with biomimetic anti-reflection layers. *Int. J. Precis. Eng. Manuf.-Green Tech.* **2017**, *4* (2), 177−181.


https://doi.org/10.1021/acsaelm.2c00035
*ACS Appl. Electron. Mater.* 2022, 4, 910−916